# Single-View 3D Human Digitalization with Large Reconstruction Models

Zhenzhen Weng[1†], Jingyuan Liu[2], Hao Tan[2], Zhan Xu[2], Yang Zhou[2]
Serena Yeung-Levy[1], Jimei Yang[2]
[1]Stanford University, [2]Adobe Research

[1]{zzweng,syyeung}@stanford.edu, [2]{jingyliu,hatan,zhaxu,yazhou,jimyang}@adobe.com
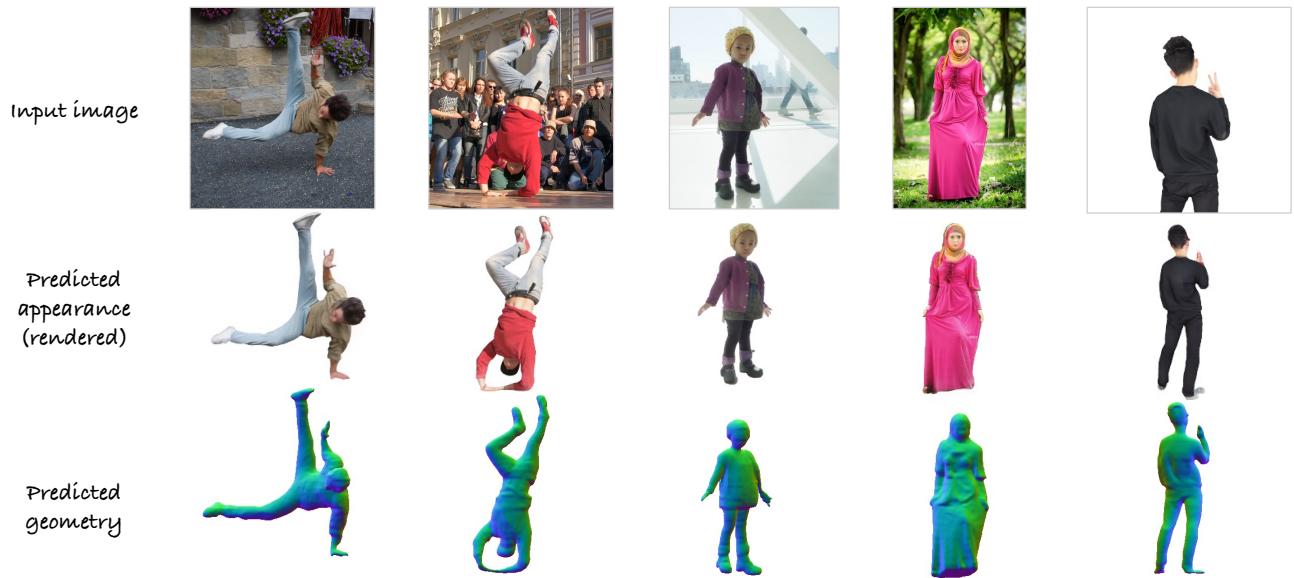
Figure 1. We present Human-LRM, a template-free large reconstruction model for feed-forward 3D human digitalization from a single image. Trained on a vast dataset comprising multi-view capture and 3D scans, our model generalizes across a broader range of scenarios. Further, equipped with a generative component, our model can generate full body humans from occluded observations. Our project webpage is at https://zzweng.github.io/humanlrm.

## Abstract

*In this paper, we introduce Human-LRM, a single-stage feed-forward Large Reconstruction Model designed to predict human Neural Radiance Fields (NeRF) from a single image. Our approach demonstrates remarkable adaptability in training using extensive datasets containing 3D scans and multi-view capture. Furthermore, to enhance the model's applicability for in-the-wild scenarios especially with occlusions, we propose a novel strategy that distills multi-view reconstruction into single-view via a conditional triplane diffusion model. This generative extension addresses the inherent variations in human body shapes when observed from a single view, and makes it possible to reconstruct the full body human from an occluded image.*

*Through extensive experiments, we show that Human-LRM surpasses previous methods by a significant margin on several benchmarks.*

## 1. Introduction

Reconstructing 3D human models from a single image is an important research topic in computer vision with an array of practical applications. These applications encompass areas such as AR/VR, asset creation, relighting , and many more. A plethora of techniques have been developed to address this challenging task, each with its own set of advantages and limitations. Parametric reconstruction methods, a.k.a. human mesh recovery (HMR) [10, 20, 46] regress pose and shape parameters of SMPL (Skinned Multi-Person Linear) human body mesh model [23], which does not include

---

[†]Work done as an intern at Adobe Research.

clothing details. This limits their utility in applications requiring realistic and detailed human representations. Conversely, implicit volume reconstruction methods [31, 32] capture fine-grained clothing details with their pixel-aligned features but do not generalize across various poses. Recent hybrid approaches [40, 41, 49] combine the advantages of parametric and implicit reconstruction methods by using the predicted SMPL body mesh as conditioning to guide the full clothed reconstruction. However, these SMPL-conditioned methods face an inevitable limitation: SMPL prediction errors propagate to the subsequent full reconstruction stage, resulting in misalignment between the reconstructed mesh and the input image. These errors are often irreparable and cannot be fully fixed by post-hoc optimization [40, 41, 49]. Lastly, these implicit reconstruction methods are hampered by the scarcity of high quality 3D scans for training.

Meanwhile, there have been various works that use NeRF [25] as a representation to learn geometry as well as texture of humans, but these work typically performs fine-tuning only on single images [1, 16], which is time consuming and not generalizable to new observations. Recently, feed-forward NeRF prediction models such as Large Reconstruction Model (LRM) [14] has been proposed, which is highly generalizable and produces high-quality 3D reconstructions as well as NeRF from arbitrary image inputs. However, directly applying pre-trained generic LRM to humans yields sub-optimal results even with fine-tuning (Figure 2). Primarily, the reconstructed surfaces tend to be coarse, not preserving enough details.

In this work, we present Human-LRM, a single-stage feed-forward model that predicts the geometry and appearance of the human from a single image. Leveraging neural radiance fields as 3D representation, we are able to scale up our training to encompass multi-view human datasets. Consequently, we are able to achieve improved generalization compared to previous methods [31, 32, 40, 41] that rely on limit 3D scan supervision. Unlike SHERF [15], an existing generalizable human NeRF prediction model that uses the predicted SMPL mesh to transform image features to the canonical space, Human-LRM is completely template-free, allowing for effective generalization in complex situations where SMPL-conditioned methods are inadequate. In contrast to LRM, Human-LRM predicts SDF values and renders with VolSDF [42] instead of classical NeRF [25], which leads to enhanced surface fidelity for final reconstruction. We additionally supervise the human geometry through normal and depth maps. These improvements prove to be effective in enabling higher quality surface reconstruction. Lastly, to address the common occlusion scenarios in the wild, we propose a novel training paradigm that distills multi-view reconstruction into single-view through conditional triplane diffusion [13, 34]. This equips Human-LRM with generative capabilities to output



Input image     Reconstructed mesh from front and side views (colored by normal)
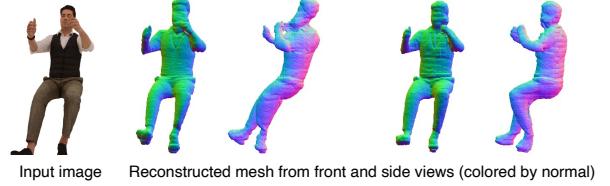
Figure 2. Limitations of LRM [14]: depth ambiguities of off-the-shelf generic LRM (left), coarse geometry even finetuning LRM on humans (right).

full body humans from partial observations (last column of Figure 1). Our contributions are summarized below:

- We introduce Human-LRM, a specialized LRM for humans with improved surface fidelity. Being trained on an extensive dataset (more than 10K shapes) with both multi-view RGB data and 3D scans, our model attains substantially enhanced generalizability and excels across a wider spectrum of scenarios and applications.
- To enhance the applicability of Human-LRM for in-the-wild scenarios, we distills multi-view Human-LRM into single-view through a conditional diffusion model. The generative Human-LRM enables better handling of unseen body parts from both other views and occlusions.
- Through extensive experiments, we show that Human-LRM outperforms previous methods significantly on a comprehensive evaluation set.

## 2. Related Work

**Parametric reconstruction.** Many 3D human reconstruction works [10, 20, 22, 46] are built on mesh-based parametric body models, e.g., SMPL [23]. Given an input image, these methods, referred as Human Mesh Recovery (HMR), employ neural networks to predict the SMPL shape and pose parameters from which the target human body mesh is constructed. This SMPL-conditioned approach greatly reduces the network output complexity and also can be adapted for weakly-supervised training with 2D pose estimates via differentiable mesh rasterization [20, 38]. As SMPL models minimally-clothed human bodies with a smooth mesh of fixed topology, it prevents these methods from reconstructing detailed geometry and texture. Nevertheless, the predicted SMPL mesh is a very good proxy for the fully clothed reconstruction as it captures the base body shape and depicts its pose structure. The promise of HMR motivates follow-up works to predict 3D offsets [2, 24, 27, 50] or build another layer of geometry on top of the base body mesh to accommodate clothed human shapes [5, 19]. However, this "body+offset" strategy lacks the flexibility to represent a wide-range of clothing types.

**Implicit reconstruction.** Implicit-functions offer a topology-agnostic representation for modeling human

shapes. PiFU [31] uses pixel-aligned image features to predict 3D occupancy values and colors from sampled 3D points in a predefined grid. Building on this, PIFuHD [32] develops a high-resolution module to predict geometric and texture details with additional front-back normal maps as input. While producing expressive reconstruction results for simple inputs like standing humans against clean background, such models are not able to generalize well to in-the-wild scenarios and often yield broken and messy shapes on challenging poses and lightings due to their limited model capacity and lack of a holistic representation.

**Hybrid reconstruction.** An emerging type of approach leverages parametric body models (e.g. SMPL [23]) to improve the generalizability of fully-supervised implicit reconstruction methods. Starting from a given image and an estimated SMPL mesh, Xiu et al. [40] regresses shapes from locally-queried features to generalize to unseen poses. Wang et al. [36] extends ICON with a GAN-based generative component. Xiu et al. [41] leverages variational normal integration and shape completion to preserve the details of loose clothing. Although the incorporation of SMPL does enhance generalizability to large poses, these methods are also constrained by the accuracy of SMPL predictions. Any errors in the estimated SMPL parameters have a cascading effect on the subsequent mesh reconstruction stage.

**Human NeRFs.** Neural Radiance Fields (NeRF) [25] marks a pivotal milestone in 3D reconstruction. NeRF empowers the learning of a 3D representation of an object solely from 2D observations. While there exist several notable works that focus on reconstructing human NeRF, these efforts often center around the single video [37] or image [16, 39] fine-tuning setting at the cost of substantial computational time, ranging from tens of minutes to hours. In contrast, our focus lies on a feed-forward paradigm that radically reduces the time required for a model to predict a human NeRF from a single image, typically in mere seconds. A few recent works [11, 21] also employ a feed-forward paradigm for generalizability, utilizing SMPL as a geometric prior and aggregating features from sparse observations, yet they necessitate multiple views. A closer related work [15] considers feed-forward human NeRF prediction from a single image. Nonetheless, their method replies on ground truth SMPL body meshes that limit their model representation power. Our method is completely template-free, opening up a broader spectrum of real-world applications, making NeRF-based human reconstruction more accessible and practical for various scenarios.

# 3. Method

An overview of Human-LRM is presented in Figure 3. Our method is built on top of LRM [14] that consists of two major building blocks: transformer-based triplane decoder and triplane NeRF. In Section 3.1, we briefly introduce triplane prediction as our model backbone and then in Section 3.2, we introduce our improved triplane NeRF to enhance the surface reconstruction quality of humans. For more details about the architecture, we refer readers to [14]. Lastly, we introduce an generative extension of our model based on on conditional diffusion, designed to complete novel views and address occlusion (Section 3.3).

## 3.1. Single-view Triplane Decoder

Given an RGB image as input, LRM first applies a pre-trained vision transformer (ViT), DINO [7] to encode the image to patch-wise feature tokens $\{\mathbf{h}_i\}_{i=1}^n \in \mathbb{R}^{768}$, where $i$ denotes the $i$-th image patch, $n$ is the total number of patches, and 768 is the latent dimension.

It then uses a transformer module to decode the image tokens into a 3D triplane [8]. Specifically, the decoder updates learnable tokens to the final triplane features via camera modulation and cross-attention with the image tokens, similar to the design of PerceiverIO [17]. More specifically, each transformer layer contains a cross-attention, a self-attention, and a multi-layer perceptron (MLP) sub-layer, where the input tokens to each sub-layer are modulated [26] by the camera features $\mathbf{c}$. The cross-attention layer attends from the triplane features to the image tokens, which can help link image information to the triplane. Then, the self-attention layer further models the intra-modal relationships across the spatially-structured triplane entries.

Triplane [8] is used as an efficient 3D representation. A triplane $\mathbf{T}$ contains three axis-aligned feature planes $\mathbf{T}_{XY}$, $\mathbf{T}_{YZ}$ and $\mathbf{T}_{XZ}$. In our implementation, each plane is of dimension $h_T \times w_T \times d_T$ where $h_T \times w_T$ is the spatial resolution, and $d_T$ is the number of feature channels. For any 3D point in the NeRF object bounding box $[-1, 1]^3$, we can project it onto each of the planes and query the corresponding point features $\mathbf{T}_{xy}$, $\mathbf{T}_{yz}$, $\mathbf{T}_{xz}$ via bilinear interpolation, which is then decoded for rendering (Section 3.2).

In short, given an input image $\mathcal{I}_1 \in \mathbb{R}^{H \times W \times 3}$, we train an encoder $\mathcal{E}$ and decoder $\mathcal{D}$ s.t. $\{\mathbf{h}_i\}_{i=1}^n = \mathcal{E}(\mathcal{I}_1)$, and $\mathbf{T}_{XY}, \mathbf{T}_{YZ}, \mathbf{T}_{XZ} = \mathcal{D}(\{\mathbf{h}_i\}_{i=1}^n, \mathbf{c})$

## 3.2. Triplane NeRF

Traditional neural volume rendering methods (as used in LRM [14]) model geometry through a generalized density function. The extraction of this geometry is achieved using a random level set of the density function, which often results in reconstructions that are noisy and of low fidelity. Hence, to improve the fidelity of the reconstructions, we predict Signed Distance Functions (SDF) instead of density. Specifically, we use two MLPs (i.e. "SDF MLP" and "RGB MLP" in Figure 3) to predict SDF and RGB from the point features queried from the triplane representation $T$. The SDF MLP takes the point features and output SDF and a latent vector $\mathbf{h}_p$. The RGB MLP takes the point features,
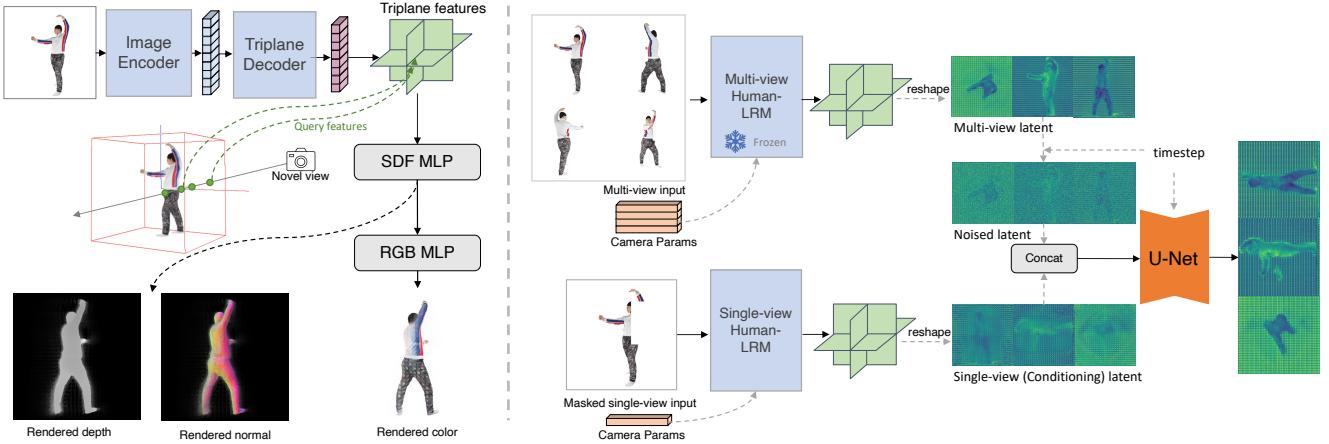
Figure 3. **Left**: Overview of single-view Human-LRM. Given a single image, we encode the image using ViT [7], and employ a transformer to decode a triplane representation [8], followed by SDF and RGB MLPs for volumetric rendering of RGB, normal and depths from novel viewpoints. **Right**: Overview of our generative Human-LRM. We first train a multi-view and a single-view Human-LRM with a shared NeRF decoder and then train a diffusion model that uses the single-view triplanes as conditioning to denoise the learned triplane from multi-view. During diffusion model training, the single view encoder takes an additional binary mask to simulate real-world occlusions.

latent vector and normals at sampled points $\hat{\mathbf{n}}_p$ (computed from predicted SDF using finite differences) and output RGB values. That is, $\mathbf{h}_p, \text{SDF} = \text{MLP}_{\text{SDF}}(\mathbf{T}_{xy}, \mathbf{T}_{yz}, \mathbf{T}_{xz})$, $\text{RGB} = \text{MLP}_{\text{RGB}}(\mathbf{T}_{xy}, \mathbf{T}_{yz}, \mathbf{T}_{xz}, \mathbf{h}_p, \hat{\mathbf{n}}_p)$. For a ray $r$ emanating from a camera position $\mathbf{o}$ in direction $\mathbf{v} \in \mathbb{R}^3$, $||\mathbf{v}|| = 1$, defined by $\mathbf{r}(t) = \mathbf{o} + t\mathbf{v}, t \geq 0$, the color of the corresponding pixel in the rendered image is computed via numerical integration

$$I(\mathbf{r}) = \sum_{i=1}^{M} \alpha_i \Pi_{i>j}(1 - \alpha_j)\text{RGB}_i, \alpha_i = 1 - e^{\sigma_i \delta_i} \quad (1)$$

where $\sigma_i$ is the density converted from SDF using [42], and $\delta_i$ is the distance between samples. Normals can be rendered using the same formula where we integrate over predicted normals at sampled points instead.

**Training objective.** Our training data contains multiple views and their respective camera parameter per human. For each human, we randomly choose a few side views, and render a random $\hat{\mathbf{x}} \in \mathbb{R}^{h \times w \times 3}$ patch on each view, similar to [37]. The ground truth RGB values for the patch is $\mathbf{x} \in \mathbb{R}^{h \times w \times 3}$. In addition, we render the predicted depths and normals of the patch $\hat{\mathbf{n}} \in \mathbb{R}^{h \times w}$ and $\hat{\mathbf{d}} \in \mathbb{R}^{h \times w \times 3}$, and supervise with depths maps $\mathbf{d} \in \mathbb{R}^{h \times w}$ and normal maps $\mathbf{n} \in \mathbb{R}^{h \times w \times 3}$. The supervising depth and normal maps can be either ground-truth renderings or off-the-shelf predictions. The training objective of our single-view reconstruction method is computed over losses from $V$ rendered views, with the input view as well as $(V - 1)$ side views.

Overall, the training objective is to minimize $\mathcal{L}$,

$$\mathcal{L} = \frac{1}{V} \sum_{v=1}^{V} (\mathcal{L}_{\text{MSE}}(\hat{\mathbf{x}}_v, \mathbf{x}_v) \quad (2)$$
$$+ \lambda_{\text{lpips}} \mathcal{L}_{\text{LPIPS}}(\hat{\mathbf{x}}_v, \mathbf{x}_v) \quad (3)$$
$$+ \lambda_n \mathcal{L}_{\text{MSE}}(\hat{\mathbf{n}}_v, \mathbf{n}_v) + \lambda_d \mathcal{L}_{\text{DSI}}(\hat{\mathbf{d}}_v, \mathbf{d}_v)) \quad (4)$$
$$+ \lambda_{eik} \mathcal{L}_{\text{Eikonal}} \quad (5)$$

Subscript $v$ means that the corresponding variable is for the $v_{th}$ supervising view. $\mathcal{L}_{\text{MSE}}$ is the normalized pixel-wise L2 loss, $\mathcal{L}_{\text{LPIPS}}$ is the perceptual image patch similarity [47], and $\mathcal{L}_{\text{DSI}}$ is the scale invariant depth loss [4]. $\mathcal{L}_{\text{Eikonal}}$ is the Eikonal regularization [12] computed using SDF values of the sampled points along the rays. $\lambda_{\text{lpips}}$, $\lambda_n$, $\lambda_d$, and $\lambda_{eik}$ are weight coefficients.

### 3.3. Conditional Diffusion Model

The above mentioned single-view deterministic model has two limitations: 1) collapsed reconstruction on the unseen parts and 2) incapability of handling occlusions. In this section, we propose a generative extension of Human-LRM with conditional diffusion. An overview of this model is illustrated in the right side of Figure 3. Specifically, we first train a multi-view reconstruction model. In contrast to the single-view model, the multi-view model incorporates camera conditioning within the ViT encoder. The triplane decoder in the multi-view model maintains the same architecture as the single-view model, with the exception that it does not take camera conditioning. With a sufficient number of views, we can conceptualize the learned triplane $\mathbf{T}^{mv}$ as a near-perfect representation of the human. We have chosen

to train a 4-view model. This decision is based on the observation that utilizing four views tends to provide a definitive and comprehensive depiction of the human subject while not excessively increasing the model's capacity. We then freeze the weights of multi-view encoder and train a single-view encoder with an additional l2 loss between the single-view and multi-view triplane features. This l2 loss has an annealing weight that starts from 0.1 to 10. For both single-view and mult-view models, we clamp the triplane features to $[-1, 1]$ using a tanh layer. To simulate real-world occlusions as well as guiding the diffusion model on which part to hallucinate, we apply a random mask to the single-view input image, and pass the binary mask to the single-view encoder through an additional mask channel.

$$\mathbf{T}^{mv} = \mathcal{D}_{mv}(\mathcal{E}_{mv}(\{\mathcal{I}_i\}_{i=1}^m), \{\mathbf{c}_i\}_{i=1}^m)) \quad (6)$$

$$\mathbf{T}^{sv} = \mathcal{D}_{sv}(\mathcal{E}_{sv}(\mathcal{I}_1 \odot \mathcal{M}_1), \mathbf{c}_1) \quad (7)$$

where $\mathcal{M}_1 \in [0, 1]^{H, W}$ is the binary mask for the single-view input image, and $m$ is the number of input views to the multi-view model.

To train a conditional model, we first flatten the predicted triplanes from the single-view model and multi-view model, yielding $\tilde{\mathbf{T}}^{sv}$ and $\tilde{\mathbf{T}}^{mv}$, each of size $(h_T \times 3, w_T, d_T)$. We then add $t$ steps of Gaussian noise to the multi-view triplane $(\tilde{\mathbf{T}}^{mv})^t$ and train a conditional diffusion model to restore $\tilde{\mathbf{T}}^{mv}$. Single-view triplane is used as conditioning, and is concatenated with the noised multi-view triplane to form the input to the diffusion model [13]. The objective of diffusion training is

$$\mathcal{L}_d = \mathbb{E}_{t \sim [1, T]}[||\tilde{\mathbf{T}}^{mv} - U_\theta((\tilde{\mathbf{T}}^{mv})^t), \tilde{\mathbf{T}}^{sv}, t)||^2] \quad (8)$$

where $t$ is the randomly sampled timestep, and $T = 1000$ is the maximum number of steps. $U_\theta$ is a UNet [30] (with weights $\theta$) that predicts the denoised multi-view triplane conditioning on single-view triplane and timestep. Note that since we changed the input channels of single-view encoder, we finetune single-view encoder during diffusion training.

## 4. Experiments

**Training data.** Our complete training set consists of 1,426 high-quality scans (500 from THuman 2.0 [44] and 926 from Alloy++), as well as around 8,000 posed multi-view captures from HuMMan [6] v1.0. THuman 2.0 and HuMMan both contain adults with simple clothing. Thus, to further evaluate the generalization capability, we collect Alloy++ from Human Alloy [3] and our internal capture. Each scan from Human Alloy has around 40K polygons and our internal capture, 100K polygons. The quality of those scans are similar to that of RenderPeople [29] (100K polygons). Alloy++ contains humans with more challenging clothing, poses, as well as little kids.

**Evaluation sets.** We evaluate on 20 humans from THuman 2.0 and 20 humans from Alloy++, each with renderings from 18 evenly spaced viewpoints. In addition, we create an evaluation set from X-Human [33]. We randomly sample 2 frames per sequence, which results in 460 frames from 20 human subjects, all with distinct poses. The X-Human testset serves as an out-of-domain evaluation set as none of the models have seen images from this dataset during training.
**Data preprocessing.** For each scan from THuman 2.0 and Alloy++, we center it by the origin and scale them so the longest side has length 1.8. We render each human scan from 32 randomly sampled viewpoints with the same camera pointing toward the origin. For HuMMan v1.0, there are 10 cameras per pose. In total, there are 16K, 14K, and 80K distinct input images from the training split of THuman 2.0, Alloy++ and HuMMan v1.0, respectively.
**Inference time.** It takes about 0.7 second for the image encoder and triplane decoder to get the triplane representation from the input image(s), and 1.3 seconds to render a 256 by 256 image from the triplanes. For our single-view conditional diffusion model, DDIM sampling with 200 steps takes about 10 seconds on a single A100 GPU.

### 4.1. Geometry Comparisons

We compare to existing single-view human reconstruction methods PiFU [31], PiFUHD [32], Pamir [49], ICON [40] and ECON [41] [1] . Since Pamir, ICON and ECON require SMPL parameters as input to their model, we use off-the-shelf SMPL predictors [10, 46] to produce them. All of these baselines require ground truth geometry as supervision and therefore their generalizability is limited by the availability of such datasets, whereas our method works with just multi-view capture, which is more accessible.

Following previous works, we report Chamfer distance, Point-to-Surface (P2S) and Normal Consistency (NC). First, we compare with their public pretrained models. As some of the baseline methods are trained on the commercially available RenderPeople, we opt for THuman 2.0, a publicly available dataset with a similar scale, to ensure a fair comparison. We train all approaches on the same dataset, to eliminate the influence of training data. While baselines use GT geometry to supervise the occupancy directly, we obtain normal and depth maps from GT geometry and use them to guide the surface prediction.

We report the quantitative results in Table 1. "Ours - SV Det." is our single-view deterministic model as described in Section 3.1. As shown by Table 1, the geometry predicted by our method consistently outperforms previous works, including works that are prior-free (PiFU and PiFUHD) as well as works that require SMPL prior (Pamir, ICON and

---
[1]Wang et al. [36] is another related work but we couldn't compare with it as there is no code release and their authors also informed us that their model checkpoints got lost.

| Model | Training Data | Requires SMPL | THuman 2.0 | | | Alloy++ | | | X-Human | | |
|---|---|---|---|---|---|---|---|---|---|---|---|
| | | | Chamfer ↓ | P2S ↓ | NC ↓ | Chamfer ↓ | P2S ↓ | NC ↓ | Chamfer ↓ | P2S ↓ | NC ↓ |
| PiFU [31] | RenderPeople-*442* | × | 6.13 | 6.18 | 0.239 | 4.97 | 5.29 | 0.207 | 5.45 | 5.65 | 0.200 |
| PiFU-HD [32] | RenderPeople-*450* | × | 6.13 | 6.08 | 0.248 | 5.51 | 5.45 | 0.229 | 5.32 | 5.13 | 0.205 |
| Pamir [49] | Twindom [35]-*900* + DeepHuman [48]-*600* | ✓ | 6.85 | 6.87 | 0.254 | 5.83 | 6.00 | 0.222 | 5.61 | 5.48 | 0.202 |
| ICON [40] | RenderPeople-*450* | ✓ | 6.59 | 6.27 | 0.245 | 4.47 | 4.43 | 0.196 | 5.48 | 5.38 | 0.197 |
| LRM [14] | Objaverse [9] + MVImgNet [45] -*730K in total* | × | 5.33 | 4.13 | 0.215 | 3.68 | 3.55 | 0.153 | 5.24 | 4.15 | 0.209 |
| Ours - SV Det. | THuman 2.0-*500*, Alloy++ -*926*, HuMMan v1.0-*8000* | × | **2.23** | **2.03** | **0.114** | **2.35** | **2.12** | **0.116** | **2.29** | **2.15** | **0.099** |
| PiFU [31] | THuman 2.0 | × | 6.15 | 6.40 | 0.247 | 4.97 | 5.30 | 0.207 | 5.43 | 5.88 | 0.206 |
| Pamir [49] | THuman 2.0 | ✓ | 6.86 | 6.56 | 0.251 | 5.81 | 5.78 | 0.217 | 5.62 | 5.34 | 0.199 |
| ICON [40] | THuman 2.0 | ✓ | 6.57 | 6.65 | 0.251 | 5.58 | 5.86 | 0.218 | 5.33 | 5.43 | 0.197 |
| ECON [41] | THuman 2.0 | ✓ | 7.14 | 6.92 | 0.247 | 5.04 | 4.64 | 0.197 | 5.87 | 5.79 | 0.200 |
| Ours - SV Det. | THuman 2.0 | × | **2.62** | **2.60** | **0.124** | **3.22** | **2.99** | **0.145** | **2.43** | **2.25** | **0.106** |

Table 1. Comparison of existing single-view reconstruction methods. Top: Comparison of off-the-shelf models. The size of each training set is *italicized*. Bottom: Fair comparison of all models on THuman 2.0.

| Model | Views | $h_T, w_T$ | Chamfer | P2S | Normal Consistency ↓ | | | |
|---|---|---|---|---|---|---|---|---|
| | | | | | Front | Side | Back | Average |
| SV Det. | 1 | 256 | 2.62 | 2.60 | 0.093 | 0.128 | 0.119 | 0.124 |
| SV Det. | 1 | 128 | 3.74 | 3.48 | 0.106 | 0.207 | 0.142 | 0.166 |
| MV Det. | 4 | 128 | 1.95 | 1.84 | 0.086 | 0.102 | 0.110 | 0.100 |
| SV Gen. | 1 | 128 | 2.28 | 2.13 | 0.093 | 0.122 | 0.118 | 0.114 |

(a) Comparison between our single-view ("SV") deterministic ("Det."), multi-view ("MV") and single-view conditioned generative ("Gen.") models on THuman 2.0.

| Model | Chamfer | P2S | Normal Consistency ↓ | | | |
|---|---|---|---|---|---|---|
| | | | Front | Side | Back | Average |
| PiFU | 9.86 | 10.54 | 0.401 | 0.352 | 0.250 | 0.339 |
| PiFU-HD | 7.32 | 7.65 | 0.31 | 0.291 | 0.201 | 0.274 |
| Pamir | 10.87 | 11.22 | 0.387 | 0.361 | 0.231 | 0.336 |
| ICON | 10.12 | 10.75 | 0.381 | 0.351 | 0.231 | 0.328 |
| ECON | 11.26 | 11.74 | 0.409 | 0.355 | 0.243 | 0.341 |
| Ours - SV Det. | 5.85 | 4.39 | 0.138 | 0.215 | 0.181 | 0.187 |
| Ours - SV Gen. | **2.36** | **2.13** | **0.101** | **0.131** | **0.130** | **0.123** |

(b) Full body reconstruction results on masked single-view images.

Table 2. Results of our generative models.

ECON). The performance of SMPL-guided works is generally affected by the errors from the predicted SMPL parameters. Even though ICON and ECON utilize an optimization algorithm to optimize the SMPL parameters to match the predicted image normals, the errors in the SMPL parameters on some images are still significant. Our method does not rely on a human mesh template such as SMPL and thus does not suffer from this problem. As shown in Figure 4, our method demonstrates exceptional generalizability to challenging cases such as people in rare poses (1st and 2nd columns) as well as little kids (last column).

## 4.2. Ablations

**Effect of GT normal and depth.** Although for our best model, we do use ground truth normal and depth maps from geometry, we can replace them with estimated ones to achieve comparable performance. We additionally experiment with supervising with predicted normals and depths from off-the-shelf predictors. While there is no notable drop in quantitative performance (Table 3), the surface details are better with GT normal and depth supervision (Figure 7).
**Effect of predicting SDF.** LRM [14] uses a single MLP to predict the density ($\sigma$) and RGB, followed by NeRF volumetric rendering (i.e. experiment "predict $\sigma$" in Table 3). We noticed that the geometry predicted by this approach tended to be more rudimentary in detail (Figure 7).
**Effect of the scale of training data.** To further showcase the increased generalization ability of our method with more training data, we train with additional training data from Alloy++ (926 scans). As shown in Table 3, our model shows the best performance, and this performance continues to enhance as we incorporate additional training data. This underscores the significance of expanding the scale of model training to improve generalizability.

## 4.3. Appearance Comparisons

Our work is closely related to generalizable NeRF SHERF [15], as we are both considering learning a feed-forward human NeRF model from a single-image without any single-image/video finetuning [37] or test-time optimization. In order to compare to SHERF [15], we train our model on HuMMan [6] and evaluate the quality of novel view renderings by SSIM, PSNR and LPIPS following the same evaluation protocol as SHERF (Table 4). The ground truth (GT) SMPL parameters utilized in SHERF are obtained through triangulation from multi-view captures. However, this process is impractical in real-world scenarios where only single-view capture is present. When we use estimated SMPL parameters from a state-of-the-art model CLIFF [22], the performance of SHERF experiences a substantial decline. This decline can be attributed to the fact that SHERF's pixel-aligned feature extraction relies heavily on the assumption that the SMPL vertices align accurately with their corresponding pixel locations. In contrast, our model does not rely on a pose prior, which makes it more resilient and adaptable for real-world scenarios. This robustness is not only demonstrated through improved quantitative results when compared to SHERF (with estimated SMPL parameters) but, more notably, through the qualitative results illustrated in Figure 6. Lastly, the surface quality from Human-LRM is significantly better than SHERF. We include visual comparisons in *Supplemental Materials*.

|  |  | THuman 2.0 | | | Alloy++ | | | X-Human | | |
| Model | Training Data | Chamfer↓ | P2S↓ | NC↓ | Chamfer↓ | P2S↓ | NC↓ | Chamfer↓ | P2S↓ | NC↓ |
|---|---|---|---|---|---|---|---|---|---|---|
| Est. d.n. | THuman 2.0, HuMMan v1.0 | 2.63 | 2.38 | 0.134 | 3.35 | 3.08 | 0.147 | 2.45 | 2.28 | 0.103 |
| No d.n. | THuman 2.0, HuMMan v1.0 | 2.63 | 2.40 | 0.132 | 3.68 | 3.20 | 0.163 | 2.75 | 2.43 | 0.117 |
| Predict $\sigma$ | THuman 2.0, HuMMan v1.0 | 2.49 | 2.32 | 0.124 | 3.48 | 3.44 | 0.156 | 2.67 | 2.59 | 0.116 |
| Full Model | THuman 2.0, HuMMan v1.0 | **2.41** | **2.21** | **0.115** | **3.16** | **2.92** | **0.145** | **2.37** | **2.21** | **0.103** |
| Small training set | THuman 2.0 | 2.62 | 2.60 | 0.124 | 3.22 | 2.99 | 0.145 | 2.43 | 2.25 | 0.106 |
| Medium training set | THuman 2.0, HuMMan v1.0 | 2.41 | 2.21 | 0.115 | 3.16 | 2.92 | 0.145 | 2.37 | 2.21 | 0.103 |
| Large training set | THuman 2.0, Alloy++, HuMMan v1.0 | **2.23** | **2.03** | **0.114** | **2.35** | **2.12** | **0.116** | **2.29** | **2.15** | **0.099** |

Table 3. Ablations of our single-view deterministic model. Top: Effect of using depth and normal maps ("d.n.") for supervision and predicting SDFs. Bottom: Effect of the scale of training data.
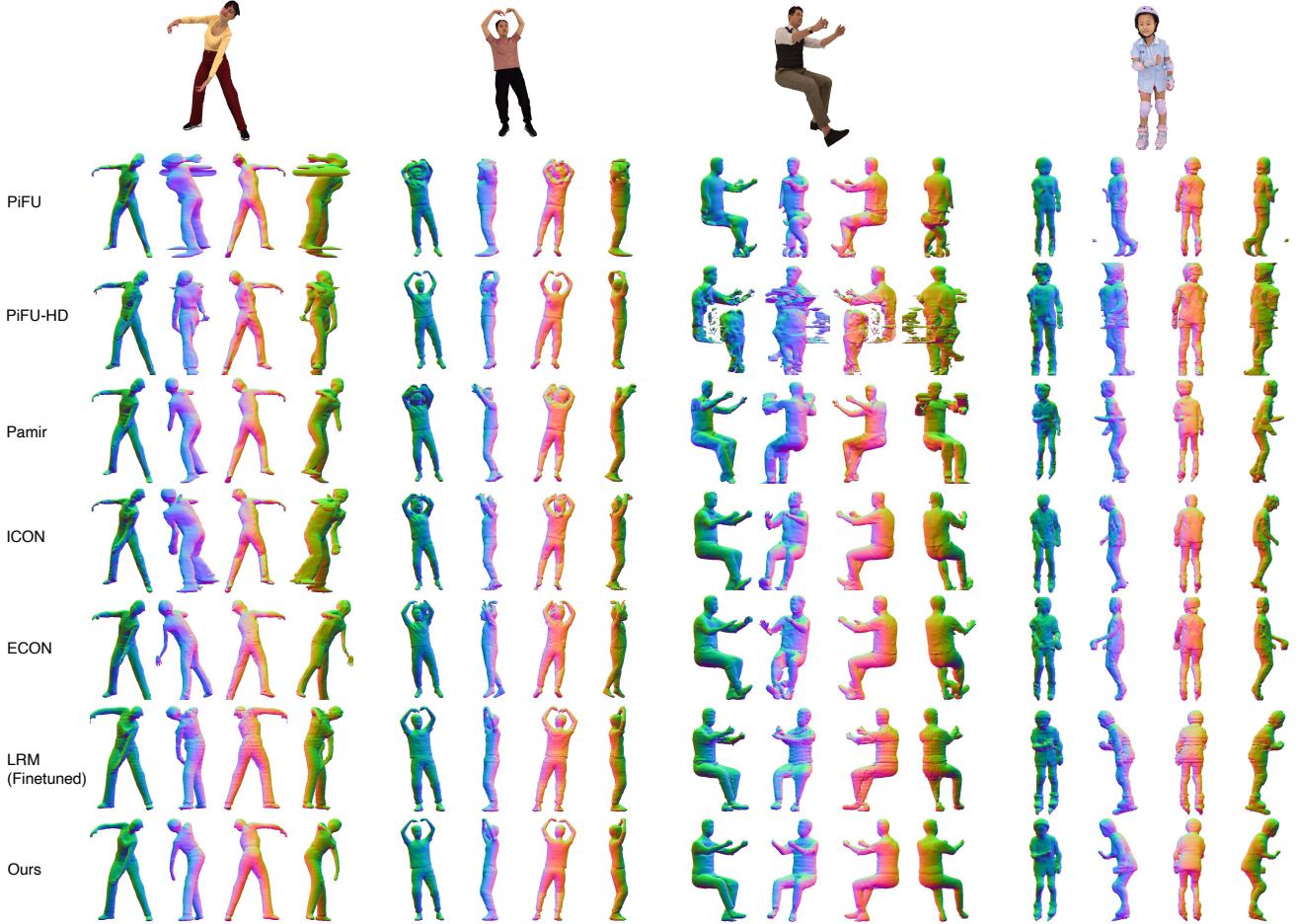


Figure 4. Comparison to previous volumetric reconstruction methods: PiFU [31], PiFUHD [32], Pamir [49], ICON [40], ECON [41], and LRM [14]. All models are trained on THuman 2.0. For each example we show the geometry (colored by mesh normals) from 4 views.

## 4.4. Generative Human-LRM Evaluation

We train a diffusion model using the single view triplane features as conditioning as described in Section 3.3. Our conditional diffusion model, enhanced with distilled information from multi-view model, is able to reconstruct credible poses from just a single viewpoint. This improves performance, particularly in scenarios where parts of the human are obscured (e.g. 1st row of Figure 5). We report quantitative performance on THuman 2.0 in Table 2a. Due to memory issues, we train the diffusion model with a smaller triplane size (128 by 128), causing the performance of the single-view model to degrade a little bit. However, we show that with the conditional diffusion, the performance of the model becomes even better than the single-view deterministic model with 256 by 256 triplanes.

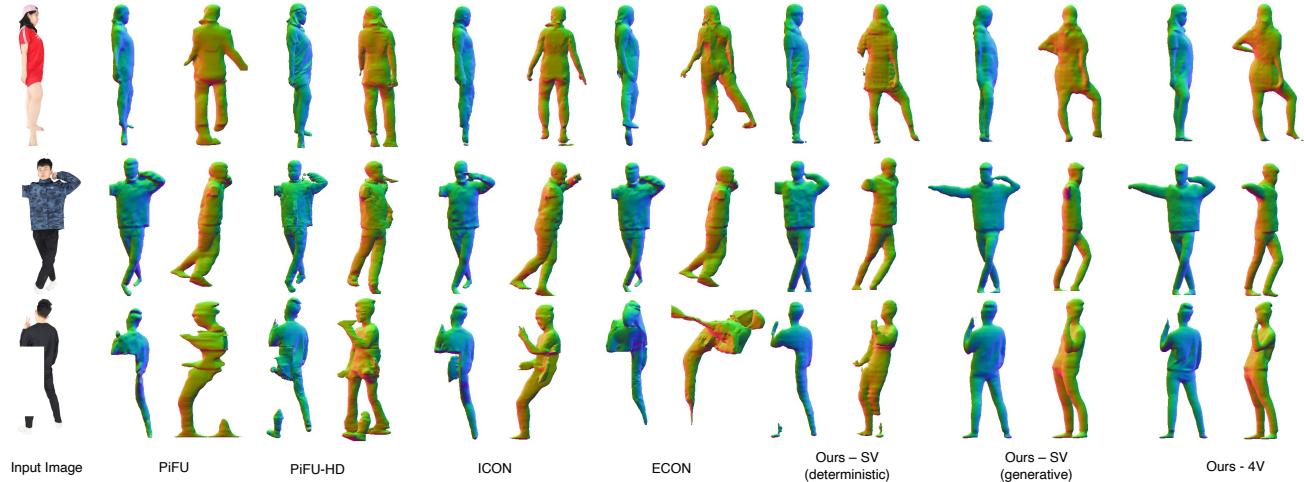In addition, our diffusion model is able to reconstruct

Figure 5. Qualitative examples of on images with occlusions. For each example we show the input view as well as side view.
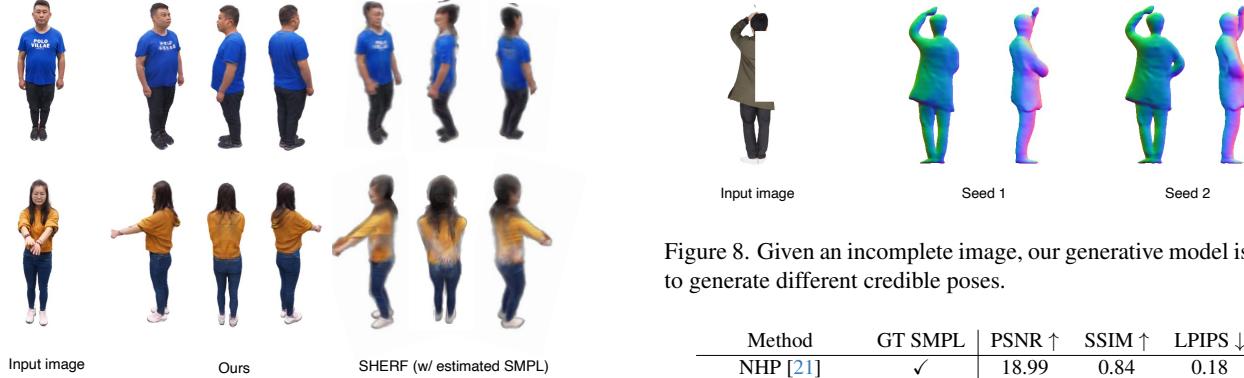


Figure 6. Novel view renderings results on HuMMan v1.0.
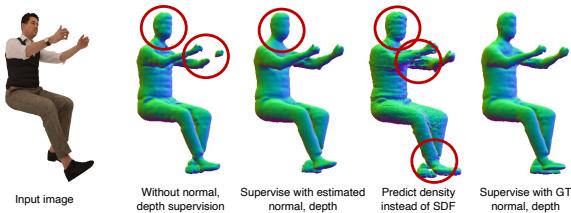


Figure 7. Ablations. We show the effect of using estimated vs. ground truth normal and depth as supervision as well as using a simple MLP as in LRM [14] to predict the density instead of SDF.



Figure 8. Given an incomplete image, our generative model is able to generate different credible poses.

| Method | GT SMPL | PSNR ↑ | SSIM ↑ | LPIPS ↓ |
|---|---|---|---|---|
| NHP [21] | ✓ | 18.99 | 0.84 | 0.18 |
| MPS-NERF [11] | ✓ | 17.44 | 0.82 | 0.19 |
| SHERF [15] | ✓ | 20.83 | 0.89 | 0.12 |
| SHERF [15] | ✗ | 14.46 | 0.79 | 0.20 |
| Ours | ✗ | 17.13 | 0.87 | 0.12 |

Table 4. Comparison to generalizable human NeRF methods on HuMMan v1.0 [6]. Top section: Feed-forward methods that use GT SMPL parameters during inference. Bottom section: methods that do not use GT SMPL during inference.

complete humans from single-view images even when the humans are occluded. In Table 2b, we randomly apply a mask to each input image to simulate real-world occlusion scenarios. Notice that all baselines fail to reconstruct the missing body part, even for SMPL-guided works like ICON and ECON that are conditioned on full-body SMPL prior. Our generative model, on the other hand, is able to halluci-

nate the occluded part (e.g. $3_{rd}$ row of Figure 5). In addition, with different random seeds, our generative model is able to reconstruct different credible poses 8.

## 5. Conclusion and Future Work

In this work, we introduced an approach for reconstructing human NeRFs from a single image. What sets our approach apart from previous implicit volumetric human reconstruction methods is its remarkable scalability, making it highly adaptable for training on large and diverse multi-view RGB datasets. This adaptability, in turn, significantly bolsters its generalizability, enabling it to surpass established baseline

models on various testsets. Additionally, our novel multi-view feature distillation approach handles inherent variations in human body capture, producing plausible and complete human geometries conditioning on a single view.

Although Human-LRM excels in capturing global geometry, it still falls short in preserving finer facial details. Future directions include utilizing more powerful representation than triplanes or potential refinement techniques.

# References

[1] Badour AlBahar, Shunsuke Saito, Hung-Yu Tseng, Changil Kim, Johannes Kopf, and Jia-Bin Huang. Single-image 3d human digitization with shape-guided diffusion. In *SIG-GRAPH Asia*, 2023. 2

[2] Thiemo Alldieck, Marcus Magnor, Bharat Lal Bhatnagar, Christian Theobalt, and Gerard Pons-Moll. Learning to reconstruct people in clothing from a single rgb camera. In *Proceedings of the IEEE/CVF Conference on Computer Vision and Pattern Recognition*, pages 1175–1186, 2019. 2

[3] Human Alloy. Human alloy, 2023. 5, 1

[4] Shariq Farooq Bhat, Reiner Birkl, Diana Wofk, Peter Wonka, and Matthias Müller. Zoedepth: Zero-shot transfer by combining relative and metric depth. *arXiv preprint arXiv:2302.12288*, 2023. 4, 1, 2

[5] Bharat Lal Bhatnagar, Garvita Tiwari, Christian Theobalt, and Gerard Pons-Moll. Multi-garment net: Learning to dress 3d people from images. In *Proceedings of the IEEE/CVF international conference on computer vision*, pages 5420–5430, 2019. 2

[6] Zhongang Cai, Daxuan Ren, Ailing Zeng, Zhengyu Lin, Tao Yu, Wenjia Wang, Xiangyu Fan, Yang Gao, Yifan Yu, Liang Pan, et al. Humman: Multi-modal 4d human dataset for versatile sensing and modeling. In *European Conference on Computer Vision*, pages 557–577. Springer, 2022. 5, 6, 8, 1

[7] Mathilde Caron, Hugo Touvron, Ishan Misra, Hervé Jégou, Julien Mairal, Piotr Bojanowski, and Armand Joulin. Emerging properties in self-supervised vision transformers. In *Proceedings of the IEEE/CVF international conference on computer vision*, pages 9650–9660, 2021. 3, 4

[8] Eric R Chan, Connor Z Lin, Matthew A Chan, Koki Nagano, Boxiao Pan, Shalini De Mello, Orazio Gallo, Leonidas J Guibas, Jonathan Tremblay, Sameh Khamis, et al. Efficient geometry-aware 3d generative adversarial networks. In *Proceedings of the IEEE/CVF Conference on Computer Vision and Pattern Recognition*, pages 16123–16133, 2022. 3, 4

[9] Matt Deitke, Dustin Schwenk, Jordi Salvador, Luca Weihs, Oscar Michel, Eli VanderBilt, Ludwig Schmidt, Kiana Ehsani, Aniruddha Kembhavi, and Ali Farhadi. Objaverse: A universe of annotated 3d objects. In *Proceedings of the IEEE/CVF Conference on Computer Vision and Pattern Recognition*, pages 13142–13153, 2023. 6

[10] Yao Feng, Vasileios Choutas, Timo Bolkart, Dimitrios Tzionas, and Michael J Black. Collaborative regression of expressive bodies using moderation. In *2021 International Conference on 3D Vision (3DV)*, pages 792–804. IEEE, 2021. 1, 2, 5

[11] Xiangjun Gao, Jiaolong Yang, Jongyoo Kim, Sida Peng, Zicheng Liu, and Xin Tong. Mps-nerf: Generalizable 3d human rendering from multiview images. *IEEE Transactions on Pattern Analysis and Machine Intelligence*, 2022. 3, 8

[12] Amos Gropp, Lior Yariv, Niv Haim, Matan Atzmon, and Yaron Lipman. Implicit geometric regularization for learning shapes. *arXiv preprint arXiv:2002.10099*, 2020. 4

[13] Jonathan Ho, Ajay Jain, and Pieter Abbeel. Denoising diffusion probabilistic models. *Advances in neural information processing systems*, 33:6840–6851, 2020. 2, 5

[14] Yicong Hong, Kai Zhang, Jiuxiang Gu, Sai Bi, Yang Zhou, Difan Liu, Feng Liu, Kalyan Sunkavalli, Trung Bui, and Hao Tan. Lrm: Large reconstruction model for single image to 3d. *arXiv preprint arXiv:2311.04400*, 2023. 2, 3, 6, 7, 8

[15] Shoukang Hu, Fangzhou Hong, Liang Pan, Haiyi Mei, Lei Yang, and Ziwei Liu. Sherf: Generalizable human nerf from a single image. *arXiv preprint arXiv:2303.12791*, 2023. 2, 3, 6, 8, 1

[16] Yangyi Huang, Hongwei Yi, Yuliang Xiu, Tingting Liao, Jiaxiang Tang, Deng Cai, and Justus Thies. Tech: Text-guided reconstruction of lifelike clothed humans. *arXiv preprint arXiv:2308.08545*, 2023. 2, 3

[17] Andrew Jaegle, Sebastian Borgeaud, Jean-Baptiste Alayrac, Carl Doersch, Catalin Ionescu, David Ding, Skanda Koppula, Daniel Zoran, Andrew Brock, Evan Shelhamer, et al. Perceiver io: A general architecture for structured inputs & outputs. *arXiv preprint arXiv:2107.14795*, 2021. 3

[18] Yasamin Jafarian and Hyun Soo Park. Learning high fidelity depths of dressed humans by watching social media dance videos. In *Proceedings of the IEEE/CVF Conference on Computer Vision and Pattern Recognition*, pages 12753–12762, 2021. 1, 2, 3

[19] Boyi Jiang, Juyong Zhang, Yang Hong, Jinhao Luo, Ligang Liu, and Hujun Bao. Bcnet: Learning body and cloth shape from a single image. In *Computer Vision–ECCV 2020: 16th European Conference, Glasgow, UK, August 23–28, 2020, Proceedings, Part XX 16*, pages 18–35. Springer, 2020. 2

[20] Angjoo Kanazawa, Michael J Black, David W Jacobs, and Jitendra Malik. End-to-end recovery of human shape and pose. In *Proceedings of the IEEE conference on computer vision and pattern recognition*, pages 7122–7131, 2018. 1, 2

[21] Youngjoong Kwon, Dahun Kim, Duygu Ceylan, and Henry Fuchs. Neural human performer: Learning generalizable radiance fields for human performance rendering. *Advances in Neural Information Processing Systems*, 34:24741–24752, 2021. 3, 8

[22] Zhihao Li, Jianzhuang Liu, Zhensong Zhang, Songcen Xu, and Youliang Yan. Cliff: Carrying location information in full frames into human pose and shape estimation. In *European Conference on Computer Vision*, pages 590–606. Springer, 2022. 2, 6

[23] Matthew Loper, Naureen Mahmood, Javier Romero, Gerard Pons-Moll, and Michael J Black. Smpl: A skinned multi-person linear model. In *Seminal Graphics Papers: Pushing the Boundaries, Volume 2*, pages 851–866. 2023. 1, 2, 3

[24] Qianli Ma, Jinlong Yang, Anurag Ranjan, Sergi Pujades, Gerard Pons-Moll, Siyu Tang, and Michael J Black. Learning to dress 3d people in generative clothing. In *Proceedings*

*of the IEEE/CVF Conference on Computer Vision and Pattern Recognition*, pages 6469–6478, 2020. 2

[25] Ben Mildenhall, Pratul P Srinivasan, Matthew Tancik, Jonathan T Barron, Ravi Ramamoorthi, and Ren Ng. Nerf: Representing scenes as neural radiance fields for view synthesis. *Communications of the ACM*, 65(1):99–106, 2021. 2, 3

[26] William Peebles and Saining Xie. Scalable diffusion models with transformers. In *Proceedings of the IEEE/CVF International Conference on Computer Vision*, pages 4195–4205, 2023. 3

[27] Gerard Pons-Moll, Sergi Pujades, Sonny Hu, and Michael J Black. Clothcap: Seamless 4d clothing capture and retargeting. *ACM Transactions on Graphics (ToG)*, 36(4):1–15, 2017. 2

[28] René Ranftl, Alexey Bochkovskiy, and Vladlen Koltun. Vision transformers for dense prediction. *CoRR*, abs/2103.13413, 2021. 1, 2

[29] RenderPeople. Renderpeople, 2018. 5

[30] Olaf Ronneberger, Philipp Fischer, and Thomas Brox. U-net: Convolutional networks for biomedical image segmentation. In *Medical Image Computing and Computer-Assisted Intervention–MICCAI 2015: 18th International Conference, Munich, Germany, October 5-9, 2015, Proceedings, Part III 18*, pages 234–241. Springer, 2015. 5

[31] Shunsuke Saito, Zeng Huang, Ryota Natsume, Shigeo Morishima, Angjoo Kanazawa, and Hao Li. Pifu: Pixel-aligned implicit function for high-resolution clothed human digitization. In *Proceedings of the IEEE/CVF international conference on computer vision*, pages 2304–2314, 2019. 2, 3, 5, 6, 7

[32] Shunsuke Saito, Tomas Simon, Jason Saragih, and Hanbyul Joo. Pifuhd: Multi-level pixel-aligned implicit function for high-resolution 3d human digitization. In *Proceedings of the IEEE/CVF Conference on Computer Vision and Pattern Recognition*, pages 84–93, 2020. 2, 3, 5, 6, 7

[33] Kaiyue Shen, Chen Guo, Manuel Kaufmann, Juan Zarate, Julien Valentin, Jie Song, and Otmar Hilliges. X-avatar: Expressive human avatars. *Computer Vision and Pattern Recognition (CVPR)*, 2023. 5, 1

[34] Jiaming Song, Chenlin Meng, and Stefano Ermon. Denoising diffusion implicit models. *arXiv preprint arXiv:2010.02502*, 2020. 2, 1

[35] Twindom. Twindom. 6

[36] Junying Wang, Jae Shin Yoon, Tuanfeng Y Wang, Krishna Kumar Singh, and Ulrich Neumann. Complete 3d human reconstruction from a single incomplete image. In *Proceedings of the IEEE/CVF Conference on Computer Vision and Pattern Recognition*, pages 8748–8758, 2023. 3, 5

[37] Chung-Yi Weng, Brian Curless, Pratul P Srinivasan, Jonathan T Barron, and Ira Kemelmacher-Shlizerman. Humannerf: Free-viewpoint rendering of moving people from monocular video. In *Proceedings of the IEEE/CVF conference on computer vision and pattern Recognition*, pages 16210–16220, 2022. 3, 4, 6

[38] Zhenzhen Weng, Kuan-Chieh Wang, Angjoo Kanazawa, and Serena Yeung. Domain adaptive 3d pose augmentation for in-the-wild human mesh recovery. In *2022 International Conference on 3D Vision (3DV)*, pages 261–270. IEEE, 2022. 2

[39] Zhenzhen Weng, Zeyu Wang, and Serena Yeung. Zeroavatar: Zero-shot 3d avatar generation from a single image. *arXiv preprint arXiv:2305.16411*, 2023. 3

[40] Yuliang Xiu, Jinlong Yang, Dimitrios Tzionas, and Michael J Black. Icon: Implicit clothed humans obtained from normals. In *2022 IEEE/CVF Conference on Computer Vision and Pattern Recognition (CVPR)*, pages 13286–13296. IEEE, 2022. 2, 3, 5, 6, 7

[41] Yuliang Xiu, Jinlong Yang, Xu Cao, Dimitrios Tzionas, and Michael J Black. Econ: Explicit clothed humans optimized via normal integration. In *Proceedings of the IEEE/CVF Conference on Computer Vision and Pattern Recognition*, pages 512–523, 2023. 2, 3, 5, 6, 7

[42] Lior Yariv, Jiatao Gu, Yoni Kasten, and Yaron Lipman. Volume rendering of neural implicit surfaces. *Advances in Neural Information Processing Systems*, 34:4805–4815, 2021. 2, 4

[43] Lior Yariv, Peter Hedman, Christian Reiser, Dor Verbin, Pratul P Srinivasan, Richard Szeliski, Jonathan T Barron, and Ben Mildenhall. Bakedsdf: Meshing neural sdfs for real-time view synthesis. *arXiv preprint arXiv:2302.14859*, 2023. 1

[44] Tao Yu, Zerong Zheng, Kaiwen Guo, Pengpeng Liu, Qionghai Dai, and Yebin Liu. Function4d: Real-time human volumetric capture from very sparse consumer rgbd sensors. In *IEEE Conference on Computer Vision and Pattern Recognition (CVPR2021)*, 2021. 5, 1

[45] Xianggang Yu, Mutian Xu, Yidan Zhang, Haolin Liu, Chongjie Ye, Yushuang Wu, Zizheng Yan, Chenming Zhu, Zhangyang Xiong, Tianyou Liang, et al. Mvimgnet: A large-scale dataset of multi-view images. In *Proceedings of the IEEE/CVF Conference on Computer Vision and Pattern Recognition*, pages 9150–9161, 2023. 6

[46] Hongwen Zhang, Yating Tian, Xinchi Zhou, Wanli Ouyang, Yebin Liu, Limin Wang, and Zhenan Sun. Pymaf: 3d human pose and shape regression with pyramidal mesh alignment feedback loop. In *Proceedings of the IEEE/CVF International Conference on Computer Vision*, pages 11446–11456, 2021. 1, 2, 5

[47] Richard Zhang, Phillip Isola, Alexei A Efros, Eli Shechtman, and Oliver Wang. The unreasonable effectiveness of deep features as a perceptual metric. In *Proceedings of the IEEE conference on computer vision and pattern recognition*, pages 586–595, 2018. 4

[48] Zerong Zheng, Tao Yu, Yixuan Wei, Qionghai Dai, and Yebin Liu. Deephuman: 3d human reconstruction from a single image. In *Proceedings of the IEEE/CVF International Conference on Computer Vision*, pages 7739–7749, 2019. 6

[49] Zerong Zheng, Tao Yu, Yebin Liu, and Qionghai Dai. Pamir: Parametric model-conditioned implicit representation for image-based human reconstruction. *IEEE transactions on pattern analysis and machine intelligence*, 44(6): 3170–3184, 2021. 2, 5, 6, 7

[50] Hao Zhu, Xinxin Zuo, Sen Wang, Xun Cao, and Ruigang Yang. Detailed human shape estimation from a single im-

age by hierarchical mesh deformation. In *Proceedings of the IEEE/CVF conference on computer vision and pattern recognition*, pages 4491–4500, 2019. 2

# Single-View 3D Human Digitalization with Large Reconstruction Models

## Supplementary Material

## A. Implementation Details

We train each of our deterministic models with 16 A100 GPUs for 7 days. We use batch size of 4 per GPU. During training, we sample rays on a random 64 by 64 patch. We use importance sampling where we sample 48 coarse and 64 fine samples along the rays. $\lambda_{lpips} = 2$, $\lambda_d = \lambda_n = 1$, $\lambda_{eik} = 0.5$. We use cosine learning rate scheduler with initial learning rate of $2e - 5$. In SDF-density conversion, we use scheduled hyper-parameters following [43] for stable optimization. The dimension of the input image is 512 by 512. For the last 3 layers of the triplane decoder, we use patch embeddings from upscaled input image (1024 by 1024) to facilitate the incorporation of higher-resolution features.

For diffusion training, we use learning rate $5e - 5$. For inference, we use DDIM [34] sampling with 200 steps. For Section 4.1 to 4.3 in the main paper, we use $h_T = w_T = 256$ and $d_T = 16$. For Section 4.4, we use $h_T = w_T = 128$ and $d_T = 64$. The diffusion model in Section 4.4 is trained on 8 A100 GPUs with learning rate $5e - 5$ for about 7 days.

## B. Comparison to SHERF's Geometry

We include additional novel view renderings results from SHERF [15] and Human-LRM on HuMMan v1.0 [6] in Figure 9. We include qualitative comparisons between SHERF's normals (computed from estimated depths) and our normal predictions. As shown, the geometry quality from Human-LRM is significantly better than SHERF.
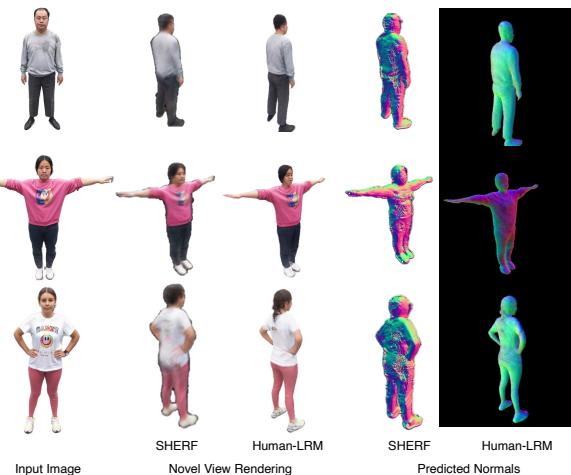


| Input Image | Novel View Rendering | Predicted Normals |
| --- | --- | --- |
| | SHERF  Human-LRM | SHERF  Human-LRM |

Figure 9. Additional comparison to SHERF.

## C. Comparison to SoTA Depth and Normal Estimation Methods

We compare the depth quality of our reconstructed geometry to state-of-the-art depth estimation works ZoeDepth [4] and DPT [28]. Furthermore, we include a comparison of the depth and normal from our predicted geometry with HD-Net [18], a method tailored for human surface reconstruction. The results (Table 5) demonstrate that our approach surpasses all baseline methods across various datasets. We include qualitative results for depth estimation in Figure 10, and normal estimation in Figure 11.

**Personal and human subjects data.** In our experiments, we use public datasets THuman 2.0 [2] [44], X-Human [3] [33], and commercially available dataset Alloy [4] [3]. These datasets are widely used for human reconstruction research and we direct to their respective website for information about their data collection procedures.

**Ethics statement.** Human-LRM is capable of transforming a single image into a 3D human. While Human-LRM's results are not yet advanced enough to deceive human perception, it's important to remain vigilant about possible ethical concerns. While we discourage such practices, there is a potential risk that the 3D human models created could be used to produce deceptive content.

---

[2] https://github.com/ytrock/THuman2.0-Dataset
[3] https://skype-line.github.io/projects/X-Avatar/
[4] https://humanalloy.com

| Method | THuman 2.0 | | Alloy ++ | | X-Human | |
|---|---|---|---|---|---|---|
| | Depth Error (↓) | Normal Error (↓) | Depth Error (↓) | Normal Error (↓) | Depth Error (↓) | Normal Error (↓) |
| DPT | 2.44 ± 0.84 | - | 2.91 ± 1.24 | - | 3.17 ± 1.20 | - |
| ZoeDepth | 2.20 ± 0.96 | - | 2.41 ± 1.01 | - | 2.08 ± 0.88 | - |
| HDNet | 2.27 ± 0.80 | 0.58 ± 0.07 | 2.37 ± 1.04 | 0.47 ± 0.06 | 2.30 ± 0.83 | 0.48 ± 0.06 |
| Human-LRM (Ours) | **0.92 ± 0.41** | **0.39 ± 0.03** | **1.79 ± 0.78** | **0.41 ± 0.05** | **1.27 ± 0.51** | **0.35 ± 0.04** |

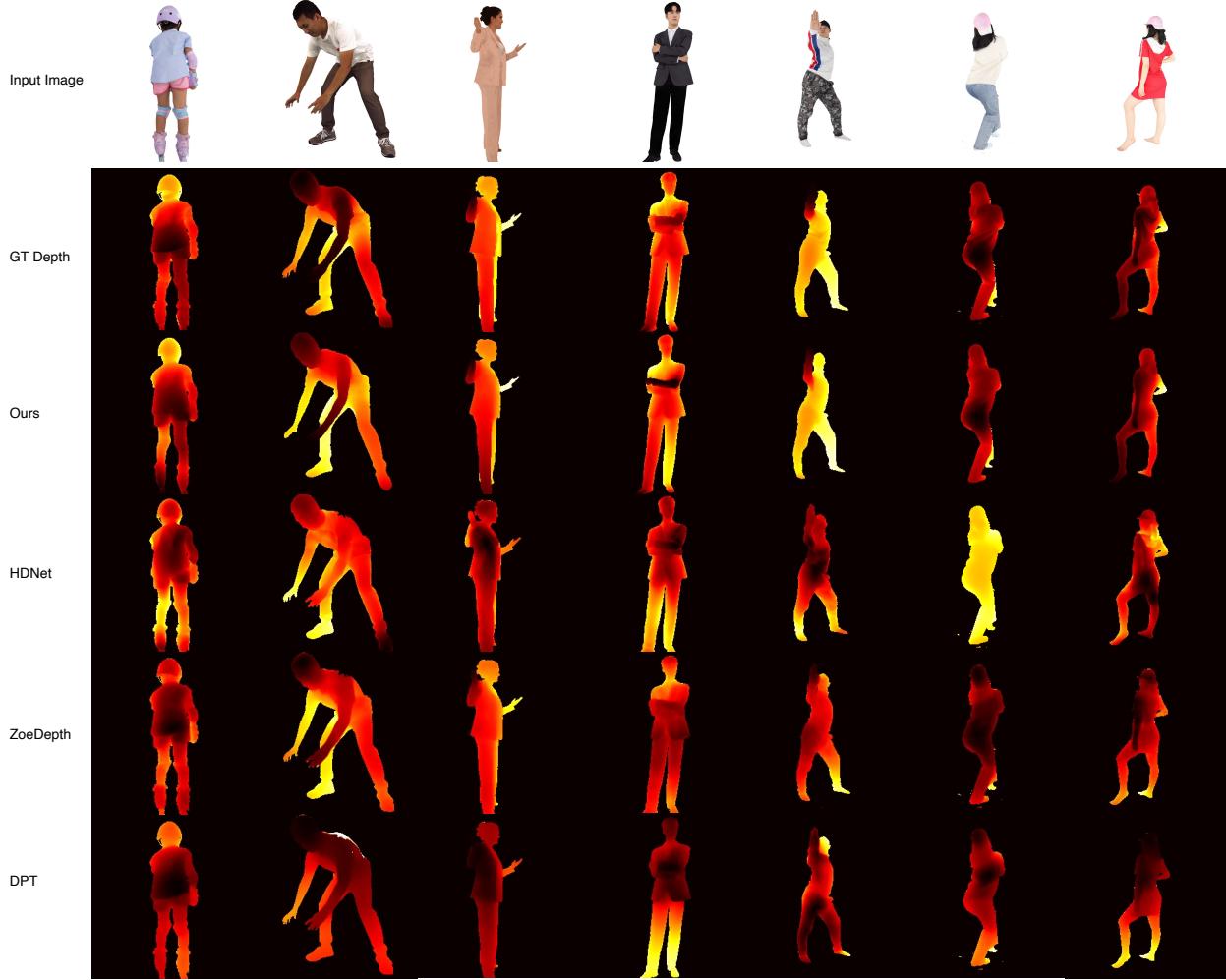Table 5. Comparison with HDNet [18], ZoeDepth [4], and DPT [28].



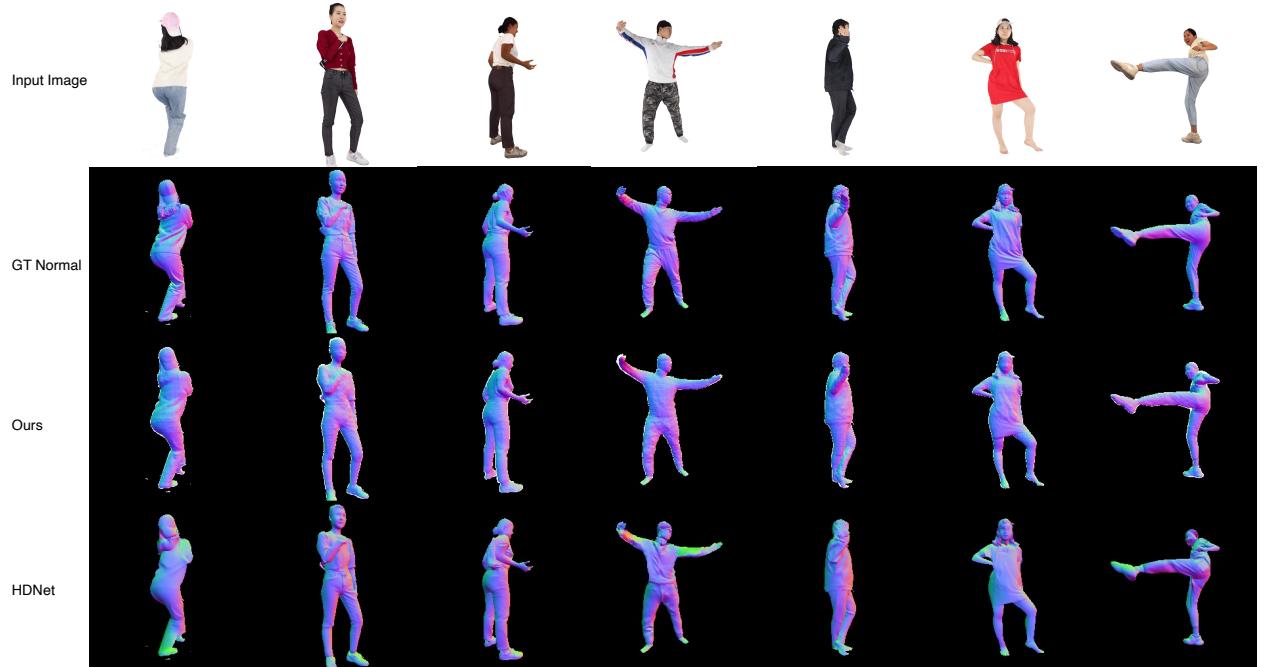Figure 10. Depth comparison to HDNet [18], ZoeDepth [4] and DPT [28]. Red color means the region is closer.

Figure 11. Normal comparison to HDNet [18].